

Strong Field Gravitational Lensing by a Kerr Black Hole

S. E. Vázquez*

*Department of Physics, University of California
Santa Barbara, California 93106-9530*

E. P. Esteban†

*Department of Physics and Astronomy MS108 Rice University 6100 Main Street
Houston, TX 77005-1892 and*

*Department of Physics, University of Puerto Rico
Humacao, Puerto Rico 00791*

(Dated: June 2, 2018)

We consider a Kerr black hole acting as a gravitational deflector within the geometrical optics, and point source approximations. The Kerr black hole gravitational lens geometry consisting of an observer and a source located far away and placed at arbitrary inclinations with respect to the black hole's equatorial plane is studied in the strong field regime. For this geometry the null geodesics equations of our interest can go around the black hole several times before reaching the observer. Such photon trajectories are written in terms of the angular positions in the observer's sky and therefore become "lens equations". As a consequence, we found for any image a simple classification scheme based in two integers numbers: the number of turning points in the polar coordinate θ , and the number of windings around the black hole's rotation axis. As an application, and to make contact with the literature, we consider a supermassive Kerr black hole at the Galactic center as a gravitational deflector. In this case, we show that our proposed computational scheme works successfully by computing the positions and magnifications of the relativistic images for different source-observer geometries. In fact, it is shown that our general procedure and results for the positions and magnifications of the images off the black hole's equatorial plane, reduce and agree with well known cases found in the literature.

PACS numbers: 95.30.Sf, 04.70.Bw, 98.62.Sb

Keywords: General Relativity, Black Holes, Gravitational Lensing

I. INTRODUCTION

As is well known, the deflection of light by a gravitating body was one of the first predictions of Einstein's General Theory of Relativity to be observationally confirmed. Later on, Einstein himself predicted what is called today a *microlens*: the momentarily increase in apparent brightness of a background star as it passes close to a foreground massive body [1]. Both the deflection of light, and the change in apparent brightness of a radiation source by an external gravitational field, are collectively known as a *gravitational lens*.

Nowadays, *gravitational lensing* is a very active area of research, and it has found applications ranging from the search of extrasolar planets and compact dark matter to estimate the value of the cosmological parameters [2, 3, 4]. In most of these applications it is only necessary to assume that the gravitational field is weak and that the deflection angle (due to a spherically symmetric body of mass M) can be approximated by: $\delta\phi \approx 4GM/bc^2$, where b is the impact parameter [5]. On the other hand, it is well known that for a Schwarzschild black hole, the deflection angle diverges as $b \rightarrow 3\sqrt{3}M$, allowing photons

to orbit the black hole many times before reaching the observer. This gives rise to an infinite set of images at both sides of the black hole [6, 7]. Notice that in this region the gravitational field is no longer weak, and the above approximation fails.

Recently, a paper by Virbhadra and Ellis have renewed interest in such images, which they called *relativistic images* [8]. Later on, Bozza [9, 10] and Eiroa, Romero and Torres [11] developed an approximation method for the case of strong *spherically-symmetric* gravitational fields. In fact, by expanding the deflection angle near the point of divergence, these authors were able to find analytic expressions for the positions and magnifications of the resulting relativistic images. Interestingly, such images were only characterized by the number of windings around the black hole [24].

Although several authors have began to study gravitational lenses with a rotating black hole as a gravitational deflector (see [12] and references therein), most of their approaches to this subject still use the weak field approximation, and focus only in null geodesic motion at the black hole's equatorial plane. In passing, we shall mention for the interested reader a nice discussion of a Kerr black hole as a gravitational lens by Bray [13]. Unfortunately, in this work there are approximations that are valid only for small deviations from the straight line path, and therefore are not suited for studying relativistic images. If we want to consider the phenomenology of

*Electronic address: svazquez@physics.ucsb.edu

†Electronic address: ep.esteban@webmail.upr.clu

the relativistic images in the strong gravitational field of a Kerr black hole, no approximations can be taken and we need to work with the full equations of motion for null rays.

There have been numerous articles about the motion of null rays in the gravitational field of a Kerr black hole [14, 15, 16, 17]. Although some of them have address the gravitational lens problem, most have concentrated in the observational effects on accretion disks and sources orbiting at the equatorial plane of the black hole and have not discussed the phenomenology of the relativistic images.

Recently, Bozza [18] studied “quasi-equatorial” orbits of photons around a Kerr black hole and provided analytical expressions for the positions and magnifications of the relativistic images. However, these approximations fail when the observer and the source are located far away from the equatorial plane. Moreover, as we show in Sec. V, Bozza’s procedure begins to fail when the black hole’s angular momentum increases near its maximum value, even if the observer and the source are close to the rotating black hole’s equatorial plane.

In this paper, we shall discuss the phenomenology of the relativistic images by using the exact null equations of motion, with the assumption that the observer and the source are far away from the black hole. Although this new procedure is far more complicated than previous works on this subject, it allow us to calculate, estimate, and discuss for the first time the observational properties of the relativistic images for arbitrary source and observer inclinations in a Kerr gravitational lens.

Therefore the purpose of this paper is two-fold. First, to extend the study of relativistic images for the case when the gravitational deflector is a rotating Kerr black hole. Secondly, since the trajectory of a photon will not always will be confined to a plane, we shall also be concerned with photon trajectories off the black hole’s equatorial plane. As a consequence of this undertaking, we show below that all relativistic images deflected by a rotating Kerr black hole are characterized by only two integers numbers: namely, the number of turning points in the polar coordinate θ , and the number of windings around the black hole’s rotation axis.

To facilitate reading this paper is divided as follows: in Sec. II to make this study self-contained a review of the null geodesic’s equations of motion in the Kerr space-time is briefly discussed. In Sec. III we explain the gravitational lens geometry, and present a general classification for all images that allow us to define formally what we mean by “relativistic images”. In Sec. IV, analytical expressions for the images’ magnification are derived. In Sec. V, we calculate the positions and magnifications of the relativistic images for several special cases, and compare our results with those in the literature. Finally, in Sec. VI a discussion of our results is undertaken. An appendix is also included to show how the null equations of motion can be solved in terms of elliptic integrals.

II. NULL GEODESICS IN THE KERR SPACE-TIME

In this section we briefly review the equations of motion for light rays in the Kerr space-time. We use the usual Boyer-Lidquist coordinates which, at infinity, are equivalent to the standard spherical coordinates. We also discuss about the relevant range of coordinates and constants of motion for the case of an observer and a source located far away from the black hole. Details about the relation between the null geodesic equations, the gravitational lens geometry, and observable quantities are given in the Sec. III.

By a convenient choice of the affine parameter, null geodesics in Kerr space-time can be described by the following first-order differential system [19]:

$$\Sigma U^r = \pm \sqrt{R(r)}, \quad (1)$$

$$\Sigma U^\theta = \pm \sqrt{\Theta(\theta)}, \quad (2)$$

$$\Sigma U^\phi = - \left(a - \frac{\lambda}{\sin^2 \theta} \right) + \frac{aP}{\Delta}, \quad (3)$$

$$\Sigma U^t = -a(a \sin^2 \theta - \lambda) + \frac{(r^2 + a^2)P}{\Delta}, \quad (4)$$

where

$$R(r) = r^4 + (a^2 - \lambda^2 - \eta)r^2 + 2[(a - \lambda)^2 + \eta]r - a^2\eta, \quad (5)$$

$$\Theta(\theta) = \eta + a^2 \cos^2 \theta - \lambda^2 \cot^2 \theta, \quad (6)$$

$$P = (r^2 + a^2) - \lambda a, \quad (7)$$

$$\Sigma = r^2 + a^2 \cos^2 \theta, \quad (8)$$

$$\Delta = r^2 - 2r + a^2. \quad (9)$$

In the above, $U^\mu = dx^\mu/d\tau$ is the four-velocity (τ is an affine parameter), λ and η are the constants of motion, $a = J/M$ is the black hole’s angular momentum per unit mass, and units are chosen such as $GM/c^2 = 1$. As is well known, for a Kerr black hole, the parameter a is restricted to $0 \leq |a| \leq 1$. From Eqs. (1) - (4) it follows that the relevant integrals of motion are

$$\int^r \frac{dr}{\pm\sqrt{R(r)}} = \int^\theta \frac{d\theta}{\pm\sqrt{\Theta(\theta)}}, \quad (10)$$

$$\Delta\phi = \int^r \frac{a(2r - a\lambda)}{\pm\Delta\sqrt{R(r)}} dr + \int^\theta \frac{\lambda}{\pm\sin^2\theta\sqrt{\Theta(\theta)}} d\theta, \quad (11)$$

$$\begin{aligned} \Delta t = & \int^r \frac{r^2(r^2 + a^2) + 2ar(a - \lambda)}{\pm\Delta[R(r)]^2} dr \\ & + \int^\theta \frac{a^2 \cos^2\theta}{\pm\sqrt{\Theta(\theta)}} d\theta. \end{aligned} \quad (12)$$

The signs of $\sqrt{R(r)}$ and $\sqrt{\Theta(\theta)}$ are those of U^r and U^θ respectively. Thus, the positive sign is chosen when the lower integration limit is smaller than the upper limit, and the negative sign otherwise.

For an observer and a source located far away from the black hole, the relevant radial integrals can be written as follows:

$$\int^r \rightarrow -\int_{r_s}^{r_{\min}} + \int_{r_{\min}}^{r_o} \approx 2 \int_{r_{\min}}^{\infty}, \quad (13)$$

where r_{\min} is the only turning point in the photon's trajectory, and it is defined by the largest positive root of $R(r) = 0$. For the angular integrals, however, there could be more than one turning point. In consequence, the most general trajectory is described by

$$\int^\theta \rightarrow \pm \int_{\theta_s}^{\theta_{\min/\max}} \pm \int_{\theta_{\min/\max}}^{\theta_{\max/\min}} \cdots \pm \int_{\theta_{\max/\min}}^{\theta_o}. \quad (14)$$

The turning points in θ are defined by $\Theta(\theta) = 0$ and are given by

$$\begin{aligned} \cos^2(\theta_{\min/\max}) = & \frac{1}{2} \left\{ 1 - \frac{\lambda^2 + \eta}{a^2} \right. \\ & \left. + \left[\left(1 - \frac{\lambda^2 + \eta}{a^2} \right)^2 + 4 \frac{\eta}{a^2} \right]^{1/2} \right\}. \end{aligned} \quad (15)$$

It is easy to show from Eq. (2) that for any pair of parameters (λ, η) , the motion in θ is bounded by θ_{\max} and θ_{\min} . Thus, the space of parameters is restricted because $\theta_{\min} \leq \theta_o, \theta_s \leq \theta_{\max}$. This constrain will be implemented in Sec. III after discussing the lens geometry. Finally, the deflection angle $\Delta\phi$ has to be chosen to satisfy a given source-observer geometry (see Sec. III for details).

Now we want to know what region of the parameter space (λ, η) correspond to photons that after reaching r_{\min} can escape to infinity. Writing Eq. (2) as

$$\eta = U_\theta^2 - a^2 \cos^2\theta + \lambda^2 \cot^2\theta, \quad (16)$$

we see that η could be negative. However, assuming a photon crosses the equator ($\theta = \pi/2$), implies that $\eta = U_\theta^2 \geq 0$. Since in this research we consider a source behind the black hole and we are mostly interested in images formed by photons that go around the black hole before reaching the observer, we will only consider the case of positive η .

For a photon to be able to return to infinity, we need $dU^r/d\tau > 0$ at $r = r_{\min}$. Setting $U^r = 0 = dU^r/d\tau$ we get:

$$\lambda(\underline{r}) = \frac{\underline{r}^2(\underline{r} - 3) + a^2(\underline{r} + 1)}{a(1 - \underline{r})}, \quad (17)$$

$$\eta(\underline{r}) = \frac{\underline{r}^3 [4a^2 - \underline{r}(\underline{r} - 3)^2]}{a^2(1 - \underline{r})^2}, \quad (18)$$

where \underline{r} is the lower bound of r_{\min} with $r_h \leq \underline{r} < \infty$, and $r_h = 1 + \sqrt{1 - a^2}$ is the Kerr black hole's horizon. This is a parametric curve in the (λ, η) space and it is shown in Fig. 1 for the case $a = 0.9$. Photons with constants of motion inside the shaded region do not have a turning point outside the horizon so they will fall into the Kerr black hole. This is analogous to the motion of

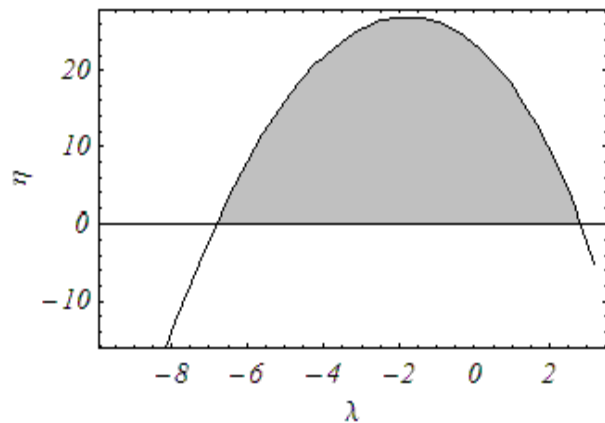


FIG. 1: Photons with parameters (λ, η) inside the shaded region will fall into the black hole. The parametric curve is for $a = 0.9$ and is defined by Eqs. (17) and (18).

null geodesics around a Schwarzschild black hole, where any photon with impact parameter $b \leq 3\sqrt{3}$ can not escape to infinity [8, 9]. This value of the parameter b , correspond to $r_{\min} = 3$ which defines the “photon sphere”. In the parameter space (λ, η) , this correspond to a close region bounded by the line $\eta = 0$ and the curve, $\sqrt{\lambda^2 + \eta} = 3\sqrt{3}$. This forbidden region in the parameter space shall be called: *photon region*. The radial integrals of Eqs. (10) and (11) diverge at the boundary of the photon region (except at the line $\eta = 0$) and take complex value inside of it. Therefore, knowledge of the mapping of this region will allow us to ensure that the equations of motion will remain well behaved.

III. THE KERR GRAVITATIONAL LENS GEOMETRY

Since Kerr space-time is asymptotically flat, an observer far away from the black hole ($r_o \gg 1$) can set up a reference euclidean coordinate system (x, y, z) with the black hole at the origin (see Fig. 2). The Boyer-Lidquist coordinates coincide with this reference frame *only for large r* . The coordinate system is chosen so that, as seen from infinity, the black hole is rotating around the z axis. For $a > 0$ the rotation will be assumed to be in the counterclockwise direction as seen from the positive z axis. Without loss of generality, we choose $\phi_o = 0$ so that the coordinates of the observers in the Boyer-Lidquist system are $(r_o, \theta_o, 0)$. Similarly, for the source we have (r_s, θ_s, ϕ_s) . In the observer's reference

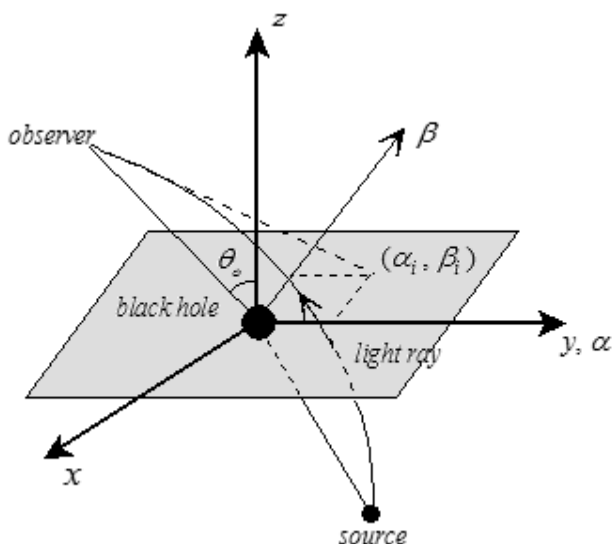


FIG. 2: Geometry of the rotating gravitational lens. An observer far away from the black hole, can set up a reference coordinate system (x, y, z) with the black hole at the origin. The Boyer-Lidquist coordinates coincide with this system only at infinity. The reference frame is chosen so that, as seen from infinity, the black hole is rotating around the z axis. In this system, the line joining the origin with the observer is normal to the α - β plane. The tangent vector to an incoming light ray defines a straight line, which intersects the α - β plane at the point (α_i, β_i) .

frame, an incoming light ray is described by a parametric curve $x(r), y(r), z(r)$, where $r^2 = x^2 + y^2 + z^2$. For large r this is just the usual radial coordinate in the Boyer-Lidquist system. At the location of the observer, the tangent vector to the parametric curve is given by: $(dx/dr)|_{r_o} \hat{x} + (dy/dr)|_{r_o} \hat{y} + (dz/dr)|_{r_o} \hat{z}$. This vector describes a straight line which intersects the α - β plane shown in Fig. 2 at (α_i, β_i) . A line joining the origin with the observer is normal to this plane. We call this plane the *observer's sky*. The point (α_i, β_i) in this plane is the point $(-\beta_i \cos \theta_o, \alpha_i, \beta_i \sin \theta_o)$ in the (x, y, z) system.

Changing to spherical coordinates and using the equations of the straight line, is easy to show that

$$\alpha_i = -r_o^2 \sin \theta_o \left. \frac{d\phi}{dr} \right|_{r_o}, \quad (19)$$

$$\beta_i = r_o^2 \left. \frac{d\theta}{dr} \right|_{r_o}. \quad (20)$$

By using Eqs. (1) - (3) in (19) and (20) and further assuming $r_o \rightarrow \infty$, it is possible to relate the constants of motion λ and η to the position of the images in the observer's sky:

$$\lambda \approx -\alpha_i \sin \theta_o, \quad (21)$$

$$\eta \approx (\alpha_i^2 - a^2) \cos^2 \theta_o + \beta_i^2. \quad (22)$$

These equations can, in turn, be written in terms of the angles (x_i, y_i) in the observer's sky by: $\alpha_i \approx r_o x_i$, $\beta_i \approx r_o y_i$. We would like to mention that Eqs. (19) - (22) are not equivalent to Eqs. (7), (8), (11) and (12) of Ref. [13]. However, our equations exactly coincide with Eqs. (28a) and (28b) of Ref. [14]. We believe that in Ref. [13], there is a calculation mistake in the intersection of the tangent to the light ray and the α - β plane. The author in Ref. [13] also ignore any contribution of the black hole's spin when expanding $(d\theta/dr)|_{r_o}$ and $(d\phi/dr)|_{r_o}$.

As can be seen later, it is also useful for our purposes to write the source's angular coordinates (θ_s, ϕ_s) in terms of its position in the observer's sky. From the geometry of Fig. 2, we obtain

$$x_s \approx \frac{r_s \sin \theta_s \cos \phi_s}{r_o - r_s (\sin \theta_o \sin \theta_s \cos \phi_s + \cos \theta_o \cos \theta_s)}, \quad (23)$$

$$y_s \approx \frac{r_s (\sin \theta_o \cos \theta_s - \cos \theta_o \sin \theta_s \cos \phi_s)}{r_o - r_s (\sin \theta_o \sin \theta_s \cos \phi_s + \cos \theta_o \cos \theta_s)}, \quad (24)$$

where (x_s, y_s) are the angles of the source in the observer's sky. Inverting Eqs. (23) and (24) for the polar and azimuthal angles, it is convenient to consider good source alignments (e.g. small x_s and y_s). The motivation for this approximation will become clear when we consider the magnifications of the relativistic images (defined below). If the observer is not exactly at $\theta_o = 0$, we can approximate: $\theta_s \approx \pi - \theta_o - \delta\theta$ and $\phi_s \approx \pi - \delta\phi$ with $\delta\theta \ll 1$ and $\delta\phi \ll 1$ (an observer exactly at $\theta_o = 0$ will be considered in Sec. V). Expanding Eqs. (23) and (24) to second order in the perturbations, one finds that

$$\theta_s \approx \pi - \theta_o - \left(1 + \frac{r_o}{r_s}\right) y_s - \frac{x_s^2 \sin 2\theta_o}{4 \left(\frac{\sin \theta_o}{1+r_o/r_s} + y_s \cos \theta_o\right)^2}, \quad (25)$$

$$\phi_s \approx \pi - \frac{x_s}{\frac{\sin \theta_o}{1+r_o/r_s} + y_s \cos \theta_o}. \quad (26)$$

Now we want to know how the restrictions in the parameter space (λ, η) and in the lens geometry are reflected in the possible values of the image coordinates (α_i, β_i) . We begin with the photon region discussed in Sec. II. This constraint correspond to a closed region in the observer's sky. It is useful to write its boundary as a parametric curve $\xi(\varphi)$, where $\xi^2 \equiv x^2 + y^2$ and $\tan \varphi \equiv y/x$. Inserting Eqs. (17), (18), (21) and (22) in the definition of φ (using the small angle approximations $\alpha \approx r_o x$, $\beta \approx r_o y$), we can solve for $\underline{r}(\varphi)$ and obtain the desired parametric curve. When doing so, one encounters a sixth order polynomial in \underline{r} . The largest positive root is valid for $-\pi/2 \leq \varphi \leq \pi/2$ and the second largest positive root for $\pi/2 \leq \varphi \leq 3\pi/2$.

Another constraint comes from the polar movement of the light rays. In Sec. II we pointed out that the motion in θ was restricted between the turning points $\theta_{\min}/\theta_{\max}$ defined by Eq. (15). Therefore, points in the parameters space where the inequality $\theta_{\min} \leq \theta_s, \theta_o \leq \theta_{\max}$ is not satisfied must be discarded.

Now we will prove that if λ and η are given by Eqs. (21) and (22), then the inequality is always satisfied for θ_o . Using the notation: $u_j \equiv \cos^2 \theta_j$, $w_j \equiv \sin^2 \theta_j$ (j is any subscript), the above inequality is equivalent to $u_m \geq u_o$ (m stands for "min/max"). In this notation, the condition for a turning point in θ , $\Theta(\theta) = 0$, becomes

$$\eta + (a^2 - \eta - \lambda^2) u_m - a^2 u_m^2 = 0. \quad (27)$$

Writing $u_m = u_o - x$ and substituting into Eq. (27), we get

$$x = \frac{1}{2a^2} \left\{ a^2 w_o - (\alpha_i^2 + \beta_i^2) \pm \sqrt{[a^2 w_o - (\alpha_i^2 + \beta_i^2)]^2 - 4a^2 \beta_i^2 w_o} \right\}. \quad (28)$$

On the other hand, using Eqs. (21) and (22) we have

$$\alpha_i^2 + \beta_i^2 = a^2 u_o + \lambda^2 + \eta. \quad (29)$$

The "radius" $\lambda^2 + \eta$ must be greater or equal than the boundary of the photon region defined by Eqs. (17) and (18) and the line $\eta = 0$. It is then easy to show that the minimum value of this "radius" is reached when $\eta = 0$ and $a = 1$. The actual minimum value is thus $(\lambda^2(\underline{r}) + \eta(\underline{r}))_{\min} = 4$. Therefore, by Eq. (29) we have that $\alpha_i^2 + \beta_i^2 \geq 4$, and since $0 \leq a^2 w_o \leq 1$, it follows the inequality

$a^2 w_o - (\alpha_i^2 + \beta_i^2) < 0$ and hence, $x \leq 0$. The equality is satisfied only for $\beta = 0$. We then can conclude that $u_m \geq u_o$.

If $u_s > u_o$, we can ensure that $u_m \geq u_s$ by doing the same construction in the frame of the source:

$$\lambda^2 = \gamma_i^2 w_s, \quad (30)$$

$$\eta = \Omega_i^2 + u_s(\gamma_i^2 - a^2), \quad (31)$$

where γ_i and Ω_i are the coordinates in the source's sky. By using Eqs. (21), (22), (30) and (31) it follows that

$$\Omega_i^2 = \beta_i^2 + \alpha_i^2 \left(\frac{u_o - u_s}{w_s} \right) + a^2(u_s - u_o), \quad (32)$$

$$\gamma_i^2 = \alpha_i^2 \frac{w_o}{w_s}. \quad (33)$$

Since for physically relevant situations we must have $\Omega_i^2 \geq 0$ (where the equality holds only for $u_m = u_s$), the excluded points will be those between the curves

$$\beta_i = \pm \left[(u_s - u_o) \left(\frac{\alpha_i^2}{w_s} - a^2 \right) \right]^{1/2}, \quad (34)$$

where $u_s \geq u_o$ and $\alpha_i^2 \geq a^2 w_s$. The forbidden regions in the observer's sky are shown in Fig. 3 for the case of $u_s > u_o$. For $u_s < u_o$, only the photon region is present.

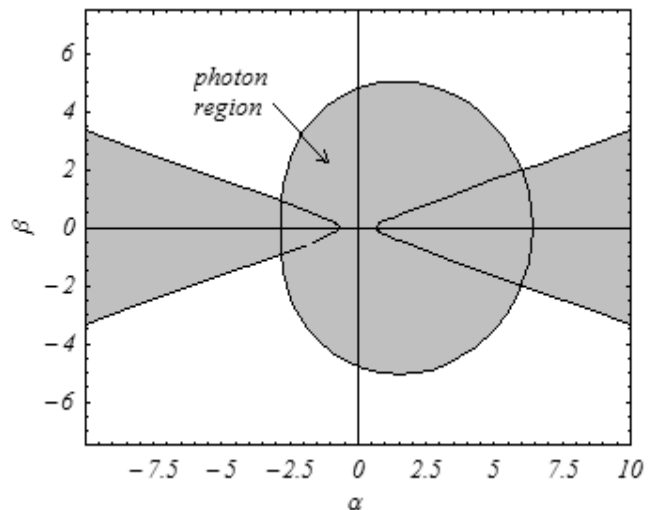


FIG. 3: Forbidden regions in the observer's sky for $u_s > u_o$. The forbidden regions are shown in shaded gray. In this case we used $a = 1$, $u_o = 1/2$ and $u_s = 1.1u_o$. For $u_s < u_o$ only the photon region is present.

Next, we focus in relating the null equations of motion considered in Sec. II with the geometry of the gravitational lens system. In the familiar case of a Schwarzschild

black hole lens, the movement of light rays is restricted to a plane. Therefore, without loss of generality we can work at the equatorial plane: $\theta = \pi/2$. Then, by substituting Eq. (10) in (11) and setting $a = 0$, we obtain the familiar Schwarzschild deflection angle:

$$\Delta\phi = 2 \int_{r_{min}}^{\infty} \frac{\lambda dr}{\sqrt{r^4 + \lambda^2 r(2-r)}}, \quad (35)$$

where $\eta = 0$ by the fact that we are working at the equatorial plane [see Eq. (16)]. This deflection angle can be written in terms x_i using Eq. (21). Then, by use of the familiar ‘‘lens equation’’ we can solve for the position of the ‘‘virtual’’ images [8]. However, another approach is to give $\Delta\phi$ in terms of the geometry of the observer-source pair and solve Eq. (35) for x_i . In this case we have

$$\Delta\phi = \begin{cases} -\phi_s - 2\pi n & , x_i > 0 \\ 2\pi(n+1) - \phi_s & , x_i < 0 \end{cases} \quad (36)$$

where $n = 0, 1, 2, \dots$ is the number of windings around the z axis. The solutions for $n = 0$ are the familiar weak field images, and for $n \geq 1$ we have the relativistic images studied in [8, 9, 10]. This last method is more useful when we consider trajectories outside the equatorial plane. In this case, Eqs. (10) and (11) with (36) become our ‘‘lens equations’’. Nevertheless, for trajectories outside the equatorial plane, an additional parameter appears: the number of turning points in the polar coordinate θ (m). For the case of the Schwarzschild black hole it is easy to prove that m is related to n as $m = 2n + 1$ by the fact that photons travel only in a plane.

What about the case of a Kerr black hole? In this situation, since the movement of light rays is not necessarily restricted to a plane, we must consider n and m as independent parameters. Additionally, in trying to write $\Delta\phi$ as in Eq. (36) one is faced with a possible complication: unlike in the Schwarzschild space-time, the Kerr geometry admits turning points in ϕ which could complicate the analysis. By using Eq. (3) with $U^\phi = 0$ is easy to show that the possible turning points occur at

$$r_{\pm}(\theta) = \frac{1}{\lambda} \left\{ (\lambda - a \sin^2 \theta) \pm \sqrt{(\lambda - a \sin^2 \theta)^2 - a^2 \lambda^2 \cos^2 \theta} \right\}. \quad (37)$$

Both solutions are surfaces of revolution around the rotation axis of the black hole. It is easy to prove that for a given λ , only one of the surfaces lies outside the horizon. Since in our case we are considering photons that come from infinity, reach a single turning point in r and return to infinity, they can cross such a surface at most in two points. In consequence, there can be at most two turning points in ϕ . However, by using Eqs. (3) and (4) for an observer and a source at large r , it is easy to prove that: $r_s^2 \sin^2 \theta_s (d\phi/dt)_s \approx \lambda \approx r_o^2 \sin^2 \theta_o (d\phi/dt)_o$ (conservation

of angular momentum). Therefore, the asymptotic sign of $d\phi/dt$ must be unchanged by the gravitational interaction. This rule out a single turning point in ϕ which would obviously change that sign. We conclude that the number of turning point in ϕ must be zero or two. In that case, the most general expression for $\Delta\phi$ is still given by Eq. (36) but with the following modification: the first case is to be use when the right hand side of Eq. (11) is negative, and the second case otherwise.

By using Eqs. (21), (22), (25) and (26), the ‘‘lens equations’’ (10) and (11) can be expressed as

$$H(x_i, y_i) - G(x_i, y_i, x_s, y_s, m) = 0, \quad (38)$$

$$\Delta\phi(x_s, y_s, n) - L(x_i, y_i) - J(x_i, y_i, x_s, y_s, m) = 0, \quad (39)$$

where H and L (G and J) are the radial (angular) integrals of Eqs. (10) and (11) respectively, and $n = 0, 1, 2, \dots$ and $m = 0, 1, 2, \dots$ are the number of windings around the z axis and the number of turning points in the polar coordinate θ respectively.

Although the integers n and m should be considered independent, as we will see in Sec. IV, the magnification does not depend directly on n . Therefore, in this paper we consider m to be the fundamental parameter. This interpretation is confirmed by our numerical results where we find that the magnification always decreases as we increase m , and for a given m , it can ever increase for images with larger n (see Sec. V).

In the familiar Schwarzschild gravitational lens, we always have two images which are formed by light rays which suffer small deviations in their trajectories. They are called *weak field images*. Additionally, we have an infinite set of faint images at both sides of the black hole [8]. These are *relativistic images*, and are the result of photons that orbit the black hole several times before reaching the observer. In Kerr space-time, where photons’ trajectories are no longer confined to a plane, the concept of ‘‘orbiting the black hole several times’’ can be subtle. For this reason, we classify images as follows: images with $m = 0, 1$ are called *direct images* (DI hereafter), and images with $m \geq 2$ are called *relativistic images* of order m (RI hereafter).

As we show in the Appendix, Eqs. (38) and (39) can be written in terms of elliptic integrals, and are highly non-linear in all arguments with the exception of n and m . Therefore, their solution require numerical and graphical methods. To solve the lens equations, we use the standard routine ‘‘FindRoot’’ build in MATHEMATICA [25]. To give an initial approximation and to ensure that a solution exist at all, we use a variety of graphical methods. Since, as we will see in Sec. V, RIs appear very near the boundary of the photon region, we found that is useful to write: $x_i = (\xi(\varphi) + \delta) \cos \varphi$ and $y_i = (\xi(\varphi) + \delta) \sin \varphi$, where $0 \leq \varphi \leq 2\pi$, $\delta \geq 0$ and $\xi(\varphi)$ is the boundary of the photon region as discussed earlier in this section. We then express all functions in terms of δ and

φ to avoid entering the photon region. We find that RIs form at very small δ . To find the images we plot the surfaces $z_1(\delta, \varphi) = H(\delta, \varphi) - G(\delta, \varphi, x_s, y_s, m)$ and $z_2(\delta, \varphi) = \Delta\phi(x_s, y_s, n) - L(\delta, \varphi) - J(\delta, \varphi, x_s, y_s, m)$ for a given source position and image numbers (n, m) . The intersection of both surfaces with the plane $z = 0$ form various curves in that plane. If the curves formed by the two surfaces intersect each other, there is a solution. Visual inspection of these curves allow us to give an initial approximation for the numerical routine. As an example, we plot part of both surfaces in Fig. 4 for $n = 3$ and $m = 4$. We usually do this for the two lowest val-

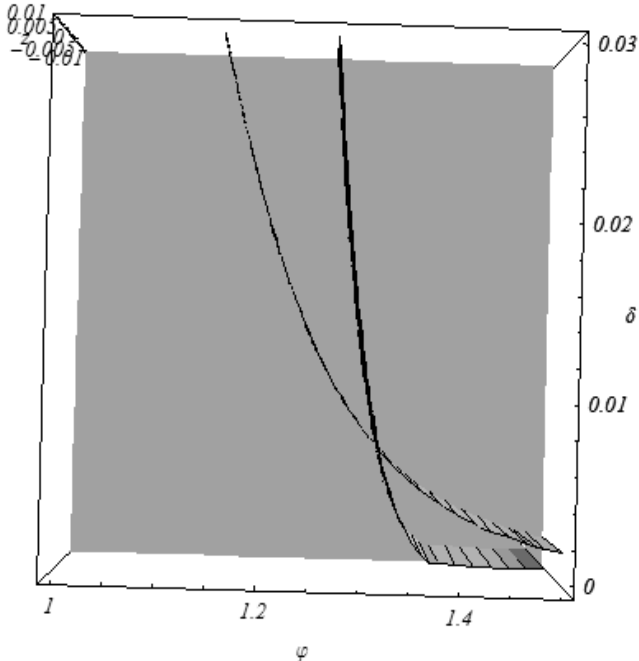


FIG. 4: Here we plot the surfaces $z_1(\delta, \varphi) = H(\delta, \varphi) - G(\delta, \varphi, x_s, y_s, m)$ and $z_2(\delta, \varphi) = \Delta\phi(x_s, y_s, n) - L(\delta, \varphi) - J(\delta, \varphi, x_s, y_s, m)$ for a source at $x_s = y_s = 1/\sqrt{2}$ arcmin, an observer at $\theta_o = \pi/4$ and for $n = 3$, $m = 4$, $a = 0.9999$. We have chosen $r_o = r_s = 8.5$ kpc as in the numerical examples of section V. The intersection of the surfaces with the $z = 0$ plane (gray) form various curves in that plane. The intersection of two such curves marks the position of a solution to the “lens equations”. The range of z has been restricted to $-0.01 \leq z \leq 0.01$ in order to clarify the intersection of the curves.

ues of m where a solution can be found. The possible values of n are bounded from above by the requirement $|\Delta\phi| \leq \max |L(\delta, \varphi) + J(\delta, \varphi, x_s, y_s, m)|$. In consequence, for a given m we usually find images for just a few values of n . This procedure is very tedious and time consuming, and for these reasons we are unable to give a complete phenomenological description of the behavior of the images for any given observer-source geometry. Instead, we shall present some numerical examples of the kind of behavior that can be expected by having a Kerr black hole as a gravitational deflector and null geodesic motion off

the equatorial plane.

As pointed out before, several authors have already obtained analytic approximations to the radial integrals in the “strong field limit” for Schwarzschild, Reissner-Nordström and Kerr black holes [9, 10, 11, 18]. Their approximations are valid for relativistic photons, with r_{\min} close to r and for small deviations from the equatorial plane in the case of the Kerr black hole. However, since in this article we are interested in orbits that can deviate significantly from the equatorial plane we can no longer use such approximation schemes. Moreover, their whole approach fail for the angular integrals because, in general, there is no relation between r_{\min} and the turning points in θ . In Sec. V, to make contact with the relevant literature, we consider trajectories close to the equatorial plane to be compared with Bozza [18] procedures.

IV. THE MAGNIFICATION IN A KERR GRAVITATIONAL LENS

The magnification of an image is defined as the ratio of the observed flux to the flux of the unlensed source. By Liouville’s theorem, the surface brightness is unchanged by the gravitational light deflection [20]. Therefore, the magnification is defined as the ratio of the solid angle subtended by the image to the solid angle of the unlensed source:

$$\mu \equiv \frac{d\omega_i}{d\omega_s} = \frac{1}{|J|}, \quad (40)$$

where J is the Jacobian of the transformation $(x_s, y_s) \rightarrow (x_i, y_i)$. Writing $x_s = x_s(x_i, y_i)$ and $y_s = y_s(x_i, y_i)$ we can find expressions for $\partial x_s/\partial x_i$, $\partial x_s/\partial y_i$, $\partial y_s/\partial x_i$ and $\partial y_s/\partial y_i$ by differentiating the lens equations (38) and (39) with respect to x_i and y_i . After some algebraic manipulations, we find that

$$\mu = \left| \frac{\alpha_1 \alpha_4 - \alpha_2 \alpha_3}{\beta_1 \beta_4 - \beta_2 \beta_3} \right|, \quad (41)$$

where

$$\alpha_1 = \frac{\partial G}{\partial x_s}, \quad \alpha_2 = \frac{\partial G}{\partial y_s}, \quad (42)$$

$$\alpha_3 = -\frac{\partial \phi_s}{\partial x_s} - \frac{\partial J}{\partial x_s}, \quad \alpha_4 = -\frac{\partial \phi_s}{\partial y_s} - \frac{\partial J}{\partial y_s}, \quad (43)$$

$$\beta_1 = \frac{\partial H}{\partial x_i} - \frac{\partial G}{\partial x_i}, \quad \beta_2 = \frac{\partial H}{\partial y_i} - \frac{\partial G}{\partial y_i}, \quad (44)$$

$$\beta_3 = \frac{\partial L}{\partial x_i} + \frac{\partial J}{\partial x_i}, \quad \beta_4 = \frac{\partial L}{\partial y_i} + \frac{\partial J}{\partial y_i}. \quad (45)$$

The above derivatives are very cumbersome and we will not expand it, neither show explicitly them here. In fact,

instead we shall use the equivalent numerical derivatives in all forthcoming calculations. Note that the magnification do not depend on n directly, since we have to take the derivative of $\Delta\phi$. Because of the complexity of these expressions, we are unable to give a complete description of the caustic structure of the Kerr space-time. Thus, we shall limit ourselves to compute the magnification of the images that we found. For a description of the caustic structure of a Kerr space-time, see [18, 21].

V. RELATIVISTIC IMAGES BY A KERR BLACK HOLE GRAVITATIONAL LENS.

In this section we present numerical calculations for the positions and magnifications of the RIs for different source-observer geometries. Our purpose is to provide a physical insight of the phenomenology that can be expected from a rotating black hole behaving as a gravitational deflector. Also, our general procedures and numerical solutions can provide a set of “test-bed” calculations for more sophisticated gravitational lens models to be developed in the near future. To be able to compare our results with recent published articles [8, 9, 10, 18] we shall consider a gravitational lens composed of a rotating black hole at the Galactic center with a mass of $M = 2.8 \times 10^6 M_\odot$, and located at a distance of $r_o = 8.5$ kpc [22]. We shall also take $r_s = r_o$.

The section is subdivided as follows: we first consider two simple cases involving a Schwarzschild black hole ($a = 0$) and an observer located at the pole ($\theta_o = 0$). Next, as a consistency check, we consider an observer at the equator ($\theta_o = \pi/2$) and compare our calculations with those of Bozza [18]. Finally, we work out a more general case of an observer at say $\theta_o = \pi/4$. The RIs are classified as follows: we use a plus (+) sign for images with sign $y_i = \text{sign } y_s$ (e.g. in the same “side” of the source) and a negative (−) sign otherwise. We do all calculations for the two lowest values of m where a solution exist. We find that, in general, images with larger m are more demagnified. The following notation will also be used: $\xi \equiv \sqrt{x^2 + y^2}$, $\varphi \equiv \arctan(y/x)$, where (x, y) are the angular positions in the observer’s sky.

In all geometric configurations considered in this section, we found that for $m = 1$ we recovered the usual weak field images without any noticeable effect from the black hole’s spin. Moreover, we could not find any image with $m = 0$ for this kind of geometry.

A. A Schwarzschild Black Hole as a Gravitational Deflector

In the Appendix we show that for $a = 0$, the angular integrals can be solved in close form. As expected, we find that the RIs are always found in the line joining the source position (x_s, y_s) and origin of the observer’s sky regardless of the inclination of the observer

θ_o . The separation ξ_i of the two outermost images is always the same regardless of the source position (or θ_o). They are: $\xi_+ = \xi_- \approx 16.952 \mu\text{arcsec}$ ($m = 3$) and $\xi_+ = \xi_- \approx 16.931 \mu\text{arcsec}$ ($m = 5$) for the two lowest order images. These results are close to those found in [8]: $\xi_+ = \xi_- \approx 16.898 \mu\text{arcsec}$ and $\xi_+ = \xi_- \approx 16.877 \mu\text{arcsec}$ respectively. The magnifications calculated by Eq. (41) are also close to those in the literature. However, we encountered problems of numerical noise when using the exact expression for $J(x_i, y_i, x_s, y_s, m)$. For that reason, to check that we obtain the right magnifications, we used the expression for $a \neq 0$ [Eq. (A.38)] and set $a \approx 10^{-11}$. The magnifications obtained this way for the outermost image as a function of the source separation agree with the literature [8]. For instance, we obtained $\mu_+ = \mu_- \approx 3.5 \times 10^{-18}$ and $\mu_+ = \mu_- \approx 3.6 \times 10^{-14}$ for $\xi_s = 1$ arcsec and $\xi_s = 100 \mu\text{arcsec}$ respectively. For comparison, in Ref. [8] we read: $\mu_+ = \mu_- \approx 3.5 \times 10^{-18}$ and $\mu_+ = \mu_- \approx 3.5 \times 10^{-14}$ respectively.

B. An Observer at the Kerr Black Hole’s Pole ($\theta_o = 0$)

Although is very unlikely that an observer will be exactly at $\theta_o = 0$, this is the simplest case that can be solved quasi-analytically. Using Eq. (21) for $\theta_o = 0$ we find that $\lambda \approx 0$. The minimum value of η , corresponding to the photon sphere, is found from Eqs. (17) and (18) by setting $\lambda = 0$. We obtain

$$\eta_{\min}(a) = \frac{r(a)^2(3r(a)^2 + a^2)}{r(a)^2 - a^2}, \quad (46)$$

where

$$r(a) = \frac{1}{3}(3 - a^2)[1 + 2 \cos(\psi/3)], \quad (47)$$

$$\tan \psi = \frac{3\sqrt{3}a\sqrt{108 - 135a^2 + 36a^4 - 4a^6}}{54 - 81a^2 + 18a^4 - 2a^6}. \quad (48)$$

Eq. (46) is a decreasing function of a satisfying $14.33 \leq \eta_{\min} \leq 27$. Since we can relate the position of the images to η by Eq. (22): $\xi_i \approx (1/r_o)\sqrt{\eta + a^2}$, Eq. (46) sets a lower bound to the separation of the images ξ_i .

The null equations of motion simplify considerable for $\lambda = 0$. First we note that from Eq. (6), there are no turning points in θ since $\eta > 0$. Therefore, the angular integration limits can be shown to be

$$p \int_0^{\pi - \theta_s} + 2(2n + 1) \int_0^{\pi/2}, \quad (49)$$

where $p = \pm 1$ is the parity of the image (− for images that are in the same side of the source when $a = 0$ and + for images in the opposite side). Here, n is the number of loops around the black hole. To relate θ_s to the unperturbed position of the source in the observer’s sky we

can no longer use the approximate expressions (25) and (26). Instead, it can be shown that

$$\theta_s \approx \pi - \xi_s \left(1 + \frac{r_o}{r_s}\right), \quad (50)$$

where we are assuming that $\xi_s(1 + r_o/r_s) \ll 1$. Now, using Eqs. (A.1), (A.4) and (A.30) given in the Appendix, the null equations of motion (10) and (11) become:

$$\begin{aligned} & \frac{4}{\sqrt{(r_a - r_c)(r_b - r_d)}} F(\psi, k) \\ & - \frac{1}{r_o \xi_i} \left\{ p F \left[\xi_s \left(1 + \frac{r_o}{r_s}\right), \frac{a^2}{r_o^2 \xi_i^2} \right] \right. \\ & \left. + 2(2n + 1) K \left(\frac{a^2}{r_o^2 \xi_i^2} \right) \right\} = 0, \quad (51) \end{aligned}$$

$$\Delta\varphi = \frac{4a}{\sqrt{(r_a - r_c)(r_b - r_d)}} \sum_{j=1}^2 \Gamma_j [(1 - \beta_j) \Pi(\psi, \alpha_j^2, k) + \beta_j F(\psi, k)], \quad (52)$$

where

$$\psi = \arcsin \sqrt{\frac{r_b - r_d}{r_a - r_d}}, \quad (53)$$

$$k^2 = \frac{(r_b - r_c)(r_a - r_d)}{(r_a - r_c)(r_b - r_d)}, \quad (54)$$

$$\alpha_i^2 = \frac{(r_j - r_b)(r_a - r_d)}{(r_j - r_a)(r_b - r_d)}, \quad (55)$$

$$\Gamma_j = \frac{\sqrt{1 - a^2} + (-1)^{j+1}}{\sqrt{1 - a^2} ((-1)^j \sqrt{1 - a^2} + r_a - 1)}, \quad (56)$$

$$\beta_j = \frac{r_j - r_a}{r_j - r_b}, \quad (57)$$

$$r_j = 1 + (-1)^{j+1} \sqrt{1 - a^2}, \quad (58)$$

and $r_a = r_{\min}$, r_b , r_c , r_d ($r_a > r_b > r_c > r_d$) are the roots of $R(r) = 0$, and Eq. (51) is valid only for $a \neq 1$ (for $a = 1$ the right hand side of Eq. (52) has to be substituted by Eq. (A.11) of the Appendix). The procedure to calculate the positions of the RIs is the following: for a given source separation ξ_s , we use Eq. (51) to calculate the angular separation of the RI (ξ_i) and then insert this value in Eq. (52) to obtain the offset from the source inclination $\Delta\varphi \equiv \varphi_i - \varphi_s$. In calculating ξ_i one has to use Eq. (46) to determine its minimum value and avoid numerical problems. Note that for $a = 0$, Eq. (51) gives $\varphi_i = \varphi_s$ as expected. In Fig. 5 we plot $\Delta\varphi$ for the three outermost images ($n = 1, 2, 3$) as a function of a for a source located at $\xi_s = 1 \mu\text{arcsec}$. The sign of $\Delta\varphi$ is that of a (which is

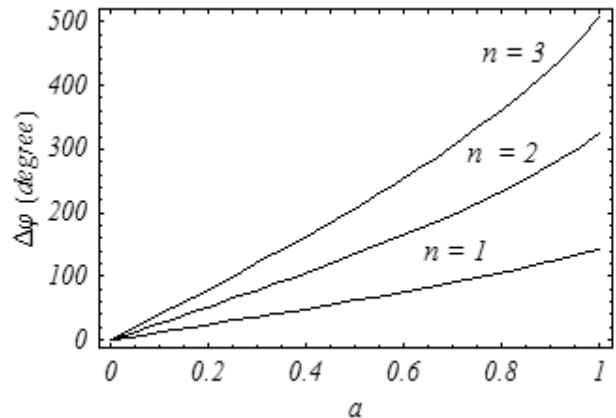


FIG. 5: Deflection in the image inclination ($\Delta\varphi \equiv \varphi_i - \varphi_s$) as a function of the normalized black hole angular momentum a . Here we consider an observer located at $\theta_o = 0$ and a source located at $\xi_s = 1 \mu\text{arcsec}$. The parameter n is the number of loops around the black hole. These plots are for $p = -1$, but photons with $p = 1$ have almost the same curves (indistinguishable within the plot resolution).

what one intuitively expects). For a given n , both images with opposite parity have almost the same $\Delta\varphi$. However, the greater the number of loops n , the greater the deflection $\Delta\varphi$ for a given a . The physical picture emerging is a very simple one: the angular momentum of the black hole just adds a “twist” in the direction of the rotation to the usual Schwarzschild trajectory. To give an intuition of the full movement of the images, including their separation ξ_i , in Fig. 6 we have plotted the position of the two lowest order images ($n = 1, 2$) as a function of the spin parameter a .

What about the magnifications? In this simple case where we have circular symmetry as seen by the observer the magnification is given by

$$\begin{aligned} \mu &= \left| \frac{\xi_i}{\xi_s} \frac{d\xi_i}{d\xi_s} \right| \\ &= \frac{\xi_i}{\xi_s} \left| \left(\frac{\partial g}{\partial \xi_s} \right) \left(\frac{\partial g}{\partial \xi_i} \right)^{-1} \right|, \quad (59) \end{aligned}$$

where $g = g(\xi_i, \xi_s)$ is the left hand side of Eq. (51). This expression for the magnification can be verified by calculating the Jacobian of the transformation $(\xi_s, \varphi_s) \rightarrow (\xi_i, \varphi_i)$. We find that, as in the Schwarzschild case, both images with the same winding number n have approximately the same magnification (to at least three significant figures). In Fig. 7 we plot the magnifications for the three lowest order images ($n = 1, 2, 3$) and with a source located at $\xi_s = 1 \mu\text{arcsec}$. The net effect of the angular momentum in this case is to enhance the brightness of the images. For the Schwarzschild case ($a = 0$), the magnifications obtained with Eq. (59) agree perfectly with the results of Ref. [8].

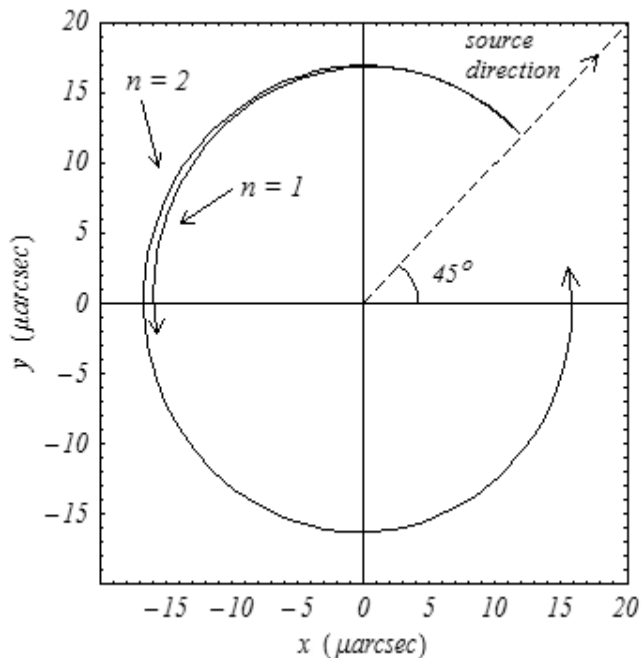


FIG. 6: Positions of the two lowest order primary RIs ($n = 1, 2$ and $p = -1$) as a function of the normalized angular momentum of the black hole a . The arrows in the curves represent the direction of the movement as we increase a from 0 to 1. The source is located at $\xi_s = 1 \mu\text{arcsec}$ and $\varphi_s = \pi/4$.

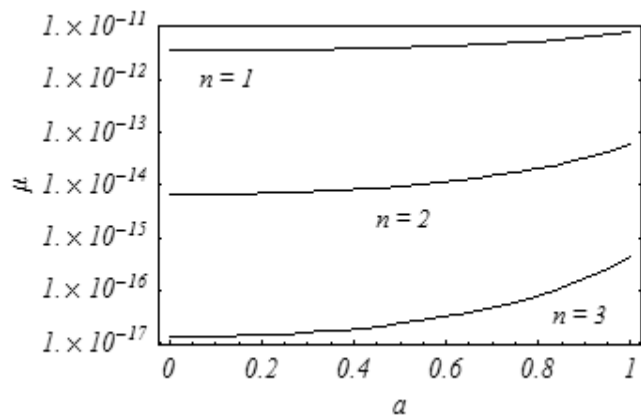


FIG. 7: Magnification for the three lowest order RIs ($n = 1, 2, 3$) for an observer at $\theta_o = 0$ and a source at $\xi_s = 1 \mu\text{arcsec}$. Here we consider the case of $p = -1$, but the magnifications for $p = 1$ are almost the same (indistinguishable in this plot).

C. An Observer at Kerr Black Hole's Equator ($\theta_o = \pi/2$)

In this subsection we consider an observer located exactly at $\theta_o = \pi/2$. Our purpose is not to give a complete account of the phenomenology of the RIs since, from an astronomical perspective, it is very unlikely that an observer will be exactly at the equator (also setting

$\theta_o = \pi/2$ does not significantly simplify our analysis). Rather than that, this special case will serve as a consistency check by allowing us to compare some of our numerical results with those of Bozza [18].

In that article, the author considered “quasi-equatorial” orbits in Kerr spacetime. One of the main approximations employed was that the horizontal position of the RIs (x_i in our notation) was calculated independently using the familiar lens equation in the equatorial plane. This, of course, assumed that the motion in ϕ was unaffected by the motion in θ . Therefore, we are forced to consider very small source declinations $\varphi_s \ll 1$. To this end (and for simplicity) we fix the source at $x_s = 1 \text{ arcsec}$ and $y_s = 1 \mu\text{arcsec}$ ($\varphi_s \approx 10^{-6}$). Then, we calculate the position and magnification of the lowest order RI in the same side of the source as a function of the spin parameter a . We fixed $n = 1$ to be consistent with the reference, where the RIs are classified only with the winding number n . We also use $a < 0$ for latter convenience. The results using the approximate equations (66), (77) and (90) of Ref. [18] and the equations of this paper are shown in Table I [26].

The general behavior of the position of this image for $a < 0$ is the following: as we increase $|a|$, it moves toward the x axis and gets very close to the forbidden region defined by Eq. (34). Then for $|a| \gtrsim 0.7$ it starts to increase φ_i until a maximum value of $\varphi_i \approx 0.1\pi$ is reached (when $|a| \rightarrow 1$). This increase in φ_i coincides with a change in the order of the image around $a \sim 0.6 - 0.7$: from $m = 3$ to $m = 2$. This illustrates the importance of considering m as an independent parameter. Also, it gives a better physical intuition of the qualitative form of the photon's trajectory (see Fig. 8).

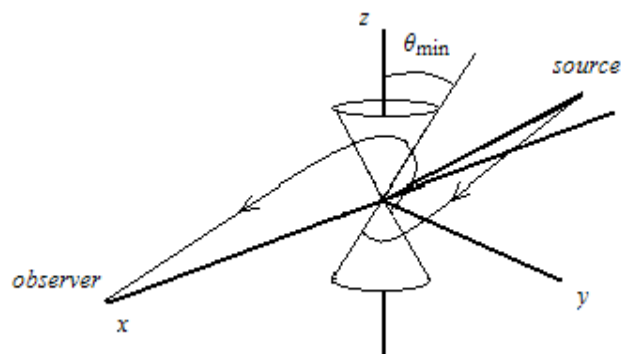


FIG. 8: A typical light ray trajectory with $m = 2$ and $n = 1$ for an observer at the equator ($\theta_o = \pi/2$). The cones represent the turning point angles $\theta_{\min/\max}$. The number of turning points in a trajectory is the number of times the photon touches these cones (in this case, two). The drawing is not to scale.

The calculations done with the approximate expressions of Bozza [18] reproduce the behavior of this RI very well until $|a|$ gets higher than $|a| \approx 0.9$ and the image moves too far away from the equator where the “quasi-

TABLE I: Here we fix the source at $\xi_s = 1$ arcsec, $\varphi_s = \pi/4$ and calculate the position and magnification of the lowest order RI in the same quadrant as the source as a function of the black hole normalized angular momentum a . The numerical results using the approximate expressions of Ref. [18] are shown in columns 2 - 4. Our results are shown in columns 5 - 8. We also show the number of turning points for each case (m). All angular positions are given in microarcseconds and all angles in radians.

a	using the formulas of Bozza			using the formulas of this paper			
	ξ_i	φ_i/π	μ	ξ_i	φ_i/π	μ	m
-10^{-6}	16.952	2.615×10^{-7}	2.9×10^{-18}	16.952	2.618×10^{-7}	2.9×10^{-18}	3
-0.1	16.295	1.442×10^{-11}	1.8×10^{-22}	16.296	1.444×10^{-11}	1.8×10^{-22}	3
-0.2	15.619	7.161×10^{-12}	1.0×10^{-22}	15.619	7.174×10^{-12}	1.1×10^{-22}	3
-0.3	14.917	4.832×10^{-12}	8.1×10^{-23}	14.918	4.844×10^{-12}	8.5×10^{-23}	3
-0.4	14.187	3.758×10^{-12}	7.4×10^{-23}	14.188	3.771×10^{-12}	7.6×10^{-23}	3
-0.5	13.422	3.223×10^{-12}	7.5×10^{-23}	13.423	3.240×10^{-12}	8.1×10^{-23}	3
-0.6	12.612	3.024×10^{-12}	8.5×10^{-23}	12.614	3.050×10^{-12}	1.8×10^{-22}	3
-0.7	11.743	3.155×10^{-12}	1.1×10^{-22}	11.747	3.207×10^{-12}	1.2×10^{-22}	2
-0.8	10.790	3.881×10^{-12}	1.6×10^{-22}	10.802	4.051×10^{-12}	1.7×10^{-22}	2
-0.9	9.695	6.672×10^{-12}	3.3×10^{-22}	9.741	8.428×10^{-12}	5.0×10^{-22}	2
-0.95	9.018	9.763×10^{-12}	4.6×10^{-22}	9.147	3.672×10^{-11}	2.8×10^{-21}	2
-0.99	8.063	4.058×10^{-12}	9.7×10^{-23}	9.042	0.1167	7.0×10^{-22}	2

equatorial” approximation is no longer valid. Choosing $a > 0$ for a source in that position would increase φ_i from the beginning and would not allow us to do the comparison with the reference.

For the magnifications, we found that our results roughly agree with those of Bozza, except for $a \gtrsim 0.9$. However, we have to admit that we encountered problems with the numerical derivatives for large values of a . Therefore, our results for this case should serve only as a order-of-magnitude estimate. Nevertheless, both results agree in that the net effect of the black hole spin is to further demagnify the RI as compared to the Schwarzschild case ($a = 0$).

D. An Observer Off the Kerr Black Hole’s Equatorial Plane ($\theta_o = \pi/4$)

This is a more general case that will allow us to illustrate the phenomenology of the RIs in a more realistic astronomical situation. We found that the general behavior of the RIs for $\theta_o = \pi/4$ is valid for a wide range of inclinations (but the precise location and magnifications of the images will depend on θ_o).

We start with a slowly rotating black hole and set $a = 10^{-6}$. We then calculate the positions and magnifications of the two lowest order RIs as a function of the source separation. More precisely, we consider a source travelling along the dashed line shown in Fig. 9. In the same figure, we show the positions of the two brightest images which correspond to $m = 3, n = 1$ in all cases. The numerical results for the two lowest order RI found are shown in Table II for $m = 3$ and Table III for $m = 5$.

Both images appear in opposite sides of the black hole as in the Schwarzschild case. However, for the slowly spinning black hole, they rotate counterclockwise as the source approaches the origin of the observer’s sky and

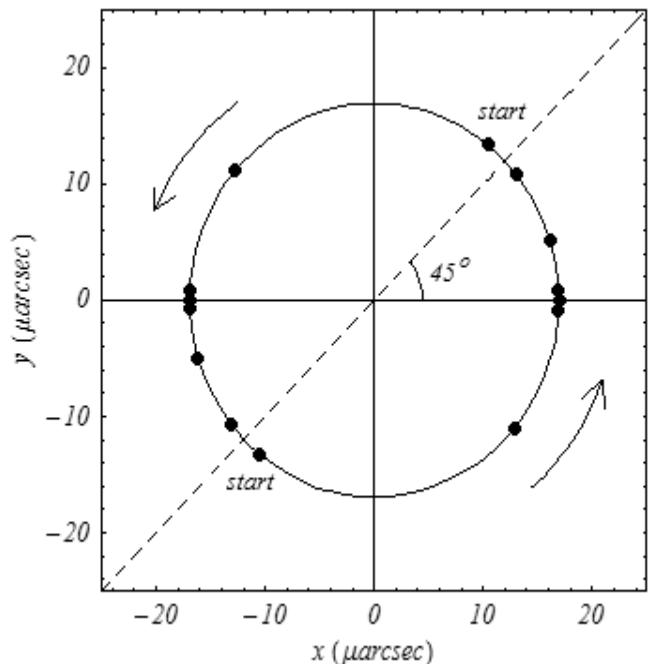


FIG. 9: Position of the lowest order RIs ($m = 3$) as a function of the source separation. The black hole spin parameter has been fixed to $a = 10^{-6}$. The source is travelling along the dashed line starting at $x_s = y_s = 1$ arcsec and finishing at $x_s = y_s = -1$ arcsec. The arrows illustrate the direction of movement of the two RIs, and their starting positions have been label by the word “start”. The solid circle is the boundary of the photon region.

emerges in the opposite quadrant (see Fig. 9). If we take $a < 0$, the effect is the same but the images rotate clockwise. Note that for very large source separations, the positions and magnifications of the images tend to the familiar Schwarzschild values [8].

TABLE II: Positions and magnifications of the lowest order RIs ($m = 3$) as a function of the source separation for a slowly rotating black hole. The spin parameter of the black hole is fixed at $a = 10^{-6}$ and the source is travelling along the dashed line of Fig. 9. Here a positive value of ξ_s means that the source is in the first quadrant of the observer's sky ($\varphi_s = \pi/4$) and a negative value means that it is located in the third quadrant ($\varphi_s = 3\pi/4$). In this case we found solutions only for $n = 1$. All angular positions are given in microarcseconds.

ξ_s	x_i^+	y_i^+	μ^+	x_i^-	y_i^-	μ^-
10^6	10.461	13.340	3.9×10^{-18}	-10.461	-13.340	3.9×10^{-18}
10^5	-12.832	11.078	3.2×10^{-17}	12.832	-11.078	3.2×10^{-17}
10^4	-16.932	0.82257	2.4×10^{-17}	16.932	-0.82260	2.4×10^{-17}
10^2	-16.952	7.8417×10^{-3}	2.3×10^{-17}	16.952	-7.8454×10^{-3}	2.3×10^{-17}
1	-16.952	6.6003×10^{-5}	2.3×10^{-17}	16.952	-6.5998×10^{-5}	2.3×10^{-17}
-1	-16.952	-9.1084×10^{-5}	2.3×10^{-17}	16.952	9.1081×10^{-5}	2.3×10^{-17}
-10^2	-16.952	-7.8631×10^{-3}	2.3×10^{-17}	16.952	7.8631×10^{-3}	2.3×10^{-17}
-10^4	-16.935	-0.74990	2.2×10^{-17}	16.935	0.75005	2.2×10^{-17}
-10^5	-16.161	-5.1170	1.5×10^{-17}	16.162	5.1154	1.5×10^{-17}
-10^6	-13.093	-10.768	3.2×10^{-18}	13.093	10.768	3.2×10^{-18}

TABLE III: Same as Table II but with $m = 5$. In this case we found solutions only for $n = 2$.

ξ_s	x_i^+	y_i^+	μ^+	x_i^-	y_i^-	μ^-
10^6	7.9844	14.930	8.1×10^{-21}	-7.9844	-14.930	8.1×10^{-21}
10^5	-16.330	4.4714	2.4×10^{-20}	16.330	-4.4714	2.4×10^{-20}
10^4	-16.927	0.37183	2.0×10^{-20}	16.927	-0.37183	2.0×10^{-20}
10^2	-16.931	3.6133×10^{-3}	2.0×10^{-20}	16.931	-3.6133×10^{-3}	2.0×10^{-20}
1	-16.931	9.3956×10^{-6}	2.0×10^{-20}	16.931	-9.3958×10^{-6}	2.0×10^{-20}
-1	-16.931	-6.3395×10^{-5}	2.0×10^{-20}	16.931	6.3396×10^{-5}	2.0×10^{-20}
-10^2	-16.931	-3.6657×10^{-3}	2.0×10^{-20}	16.931	3.6657×10^{-3}	2.0×10^{-20}
-10^4	-16.927	-0.35624	1.9×10^{-20}	16.927	0.35624	1.9×10^{-20}
-10^5	-16.672	-2.9498	1.6×10^{-20}	16.672	2.9498	1.6×10^{-20}
-10^6	-13.984	-9.5443	5.2×10^{-21}	13.984	9.5443	5.2×10^{-21}

If we compare the magnifications with those calculated in Ref. [8] for a source at the same separations but with $a = 0$ (Schwarzschild black hole), we again observe that the effect of the black hole spin is to further demagnify the RIs. For instance, for a source at $\xi_s = 1 \mu\text{arcsec}$, the magnifications calculated in [8] for the two brightest RIs were: $\mu_+ = \mu_- \approx 3.5 \times 10^{-12}$ while our calculations for $a = 10^{-6}$ yield $\mu_+ = \mu_- \approx 2.3 \times 10^{-17}$, a difference of five orders of magnitude! A similar behavior is observed for $m = 5$ (see Table III). This example illustrates how even a small value of a can make significant differences in the phenomenology of the strong-field gravitational lens.

Now we consider a fixed source at $\xi_s = 1 \text{ arcsec}$, $\varphi_s = \pi/4$ and calculate the positions and magnifications of the two lowest order RIs as a function of the spin parameter a . We consider the case of $a > 0$ only for simplicity. To illustrate the phenomenology of the RIs we have included Fig. 10. We observe that for $10^{-6} \lesssim a \lesssim 10^{-3}$ the two lowest order sets of RIs have $m = 3$ and $m = 5$ respectively as in the case of a Schwarzschild black hole. We also observe two images per value of m . As we increase a , these images move toward the x axis of the observer's sky. For $a \gtrsim 10^{-2}$ these images disappear in the x axis and give rise to images of order $m = 2$ and $m = 4$. For $m = 2$, we observe only one image in the third quadrant of the observer's sky. On the other hand, for $m = 4$

we found two images (one in the first quadrant and one in the third). Increasing a even more ($a = 0.9999$) we discovered that for $m = 2$, two images are formed in the third quadrant while for $m = 4$, a total of six images are observed: two in the first quadrant and four in the third quadrant. The positions of the lowest order images ($m = 2$ and $m = 3$) are shown in Fig. 10 while the position and magnifications of all images ($m = 2, 3, 4, 5$) are listed in Tables IV - VII. It is interesting how the number and order of the images depend on the value of the spin parameter a .

With regard to the magnifications, we observe that as in previous cases, the effect of the black hole angular momentum is to demagnify the images (although there is a slight increase in the magnification for $a = 0.9999$). Also note that the images with $m = 4$ in the first quadrant have magnifications very similar to those with $m = 2$ (located in the third quadrant). Therefore, these images should be considered "dual" to each other since they form the pair of brightest images for a given value of a ($a \gtrsim 10^{-2}$). An interesting consequence of the black hole rotation is that for large values of a ($a \gtrsim 0.1$) the two brightest images have different magnifications. This is to be compared to the case of a Schwarzschild black hole where the two brightest RIs have exactly the same magnification. Also, for large a the RIs are very static as

TABLE IV: Positions and magnification of the order $m = 3$ RIs as a function of the black hole spin parameter a . Here we consider a fixed source at $\xi_s = 1$ arcsec and $\varphi_s = \pi/4$. For $a \gtrsim 10^{-2}$ these images disappear in the x axis of the observer's sky. All images have $n = 1$. All angular positions are given in microarcseconds.

a	x_i^+	y_i^+	μ^+	x_i^-	y_i^-	μ^-
10^{-6}	10.461	13.340	3.9×10^{-18}	-10.4605	-14.930	3.9×10^{-18}
10^{-5}	-12.832	11.077	3.2×10^{-18}	12.8318	-11.0777	3.2×10^{-18}
10^{-4}	-16.932	0.82137	2.4×10^{-19}	16.9326	-0.82145	2.4×10^{-19}
10^{-3}	-16.947	0.066386	2.3×10^{-20}	16.9565	-0.0664584	2.3×10^{-20}

TABLE V: Same as Table IV but with $m = 5$. All images have $n = 2$.

a	x_i^+	y_i^+	μ^+	x_i^-	y_i^-	μ^-
10^{-6}	7.9844	14.930	8.1×10^{-21}	-7.9844	-14.930	8.1×10^{-21}
10^{-5}	-16.330	4.4712	2.4×10^{-21}	16.330	-4.4713	2.4×10^{-21}
10^{-4}	-16.926	0.36919	2.0×10^{-22}	16.927	-0.36923	2.0×10^{-22}
10^{-3}	-16.926	9.5138×10^{-3}	2.0×10^{-23}	16.935	-9.5469×10^{-3}	2.0×10^{-23}

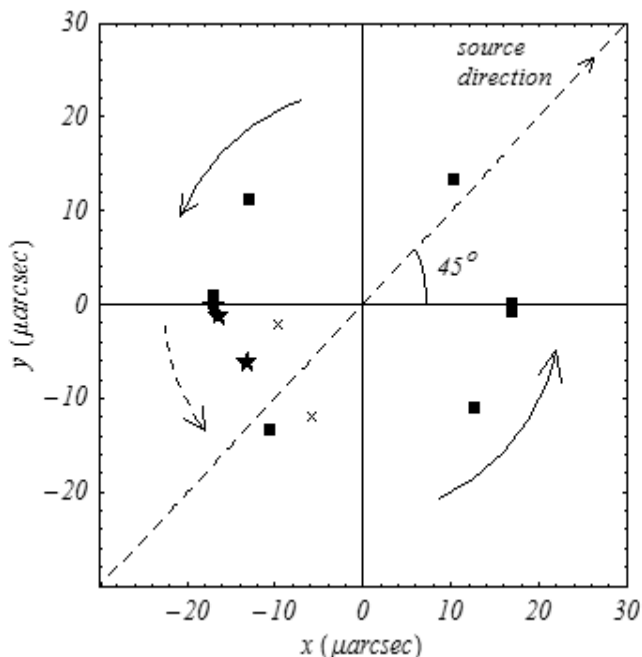


FIG. 10: In this plot we show the position of the lowest order RIs as a function of the normalized angular momentum a . The source is fixed at $\xi_s = 1$ arcsec, $\varphi_s = \pi/4$. While we increase the angular momentum starting from $a = 10^{-6}$, two images with $m = 3$ (boxes, \blacksquare) move toward the x axis as indicated by the solid arrows. Increasing a further ($a \gtrsim 10^{-2}$), these images disappear in the x axis and give rise to a single $m = 2$ image (stars, \star) that move as indicated by the dashed arrow. For $a = 0.9999$ we find two images with $m = 2$ in the third quadrant of the observer's sky (crosses, \times).

in the Schwarzschild case (although for $a = 0$ they have $\varphi_i = \varphi_s$). In other words, their positions do not depend on the location of the source.

What is even more surprising is that for $a \neq 0$ and within our numerical precision, it seems that the ratio of

the magnifications of the two brightest RIs is insensitive to the position of the source. This raises the possibility of extracting information about the orientation and spin of the black hole by comparing the brightness of this two images. However, to move this proposal forward we would need to study the behavior of the ratio of their magnifications for different values of θ_o . We do not attempt to carry such analysis this time. We hope that any new approximation scheme developed in the future can allow us to address that question.

VI. CONCLUSIONS

In this article we have explored the phenomenology of strong field gravitational lensing by a Kerr black hole. In particular we have developed a general procedure to calculate the positions and magnification of all images for an observer and source far away from the black hole and at arbitrary inclinations. We have applied our developed procedure to the case of a black hole at the Galactic center with mass $M = 2.8 \times 10^6 M_\odot$ and at a coordinate distance of $r_o = 8.5$ kpc. We have reproduced the positions and magnifications of the lowest order relativistic images found in the references for a Schwarzschild black hole and for “quasi-equatorial” trajectories around a Kerr black hole. We have also presented new numerical results for the case of an observer located at $\theta_o = \pi/4$.

Although we have not been able to give a full account of the phenomenology for all possible combination of the source-observer geometry and the spin parameter a , our limited results were useful to get a physical insight of the effects of the black hole angular momentum in the strong-field regime of gravitational lensing. Moreover, our findings can serve as a “test-bed” calculation for any improved new model of gravitational lens.

There is no doubt that observations of the strong-field regime of gravitational lensing will be an extremely challenging task in the near future. This is because, as we

TABLE VI: Positions and magnifications of the order $m = 2$ images as a function of the spin parameter a . Here we consider a fixed source at $\xi_s = 1$ arcsec and $\varphi_s = \pi/4$. These images appear for $a \gtrsim 10^{-2}$. Note that for the first three values of a we have only one image but for $a = 0.9999$ there are two images. Also, in this case we found images with different values of n ($n = 1, 2$). All angular positions are given in microarcseconds.

a	x_i^-	y_i^-	μ^-	n
10^{-2}	-16.906	-0.11746	2.3×10^{-21}	1
0.1	-16.439	-1.2457	2.5×10^{-22}	1
0.5	-13.200	-6.1999	8.3×10^{-23}	1
0.9999	-5.9311	-11.907	1.1×10^{-22}	1
	-9.6208	-2.0417	1.1×10^{-22}	2

TABLE VII: Same as Table VI but with $m = 4$. Note that in this case we have two images for the first three values of a , but six images for $a = 0.9999$. Also, we find images with $n = 1 - 7$.

a	x_i^+	y_i^+	μ^+	n	x_i^-	y_i^-	μ^-	n
10^{-2}	16.997	0.11757	2.3×10^{-21}	1	-16.883	-0.26620	2.0×10^{-24}	2
0.1	17.354	1.2638	2.1×10^{-22}	1	-16.244	-2.6972	2.6×10^{-25}	2
0.5	17.680	6.6724	3.8×10^{-23}	1	-7.7361	-13.392	2.4×10^{-25}	2
0.9999	9.1375	15.830	8.1×10^{-23}	1	-6.6670	-10.505	6.5×10^{-25}	3
					-8.5479	-6.5516	8.2×10^{-25}	4
					-9.0293	-4.2960	1.1×10^{-24}	5
					-9.1975	-2.6233	1.7×10^{-24}	6
					-9.2611	-0.93129	6.5×10^{-24}	7
					3.4194	16.348	7.5×10^{-23}	1

have seen, the relativistic images are always highly demagnified. However, if we are able to observe them in any foreseeable future, they will provide one of the best tests of Einstein's General Theory of Relativity in strong gravitational fields. Moreover, as we have seen, they could provide new tools to astrophysics by allowing the measurement of the orientation and/or magnitude of the angular momentum of the black hole. However, to fully confirm that this is the case, more research is needed toward developing an analytical solution of the strong-field gravitational lens problem in Kerr space-time.

Acknowledgments

S. E. Vázquez is very grateful to E. P. Esteban for all his support and advise during his undergraduate years. He would also like to thank NSF for a Graduate Research Fellowship and the University of California at Santa Barbara for a Broida Excellence Fellowship. E. P. Esteban thanks the support given by UPR-Humacao and Rice university during his sabbatical leave.

APPENDIX

Here we show how to write Eqs. (10) and (11) in terms of elliptic integrals. All derivations are done following Ref. [23].

1. Radial integrals

We start with the radial integral of Eq. (10):

$$\begin{aligned}
 H(\lambda, \eta) &\equiv 2 \int_{r_{\min}}^{\infty} \frac{dr}{\sqrt{R(r)}} \\
 &= \frac{4}{\sqrt{(r_a - r_c)(r_b - r_d)}} F(\psi, k), \quad (\text{A.1})
 \end{aligned}$$

where $F(\psi, k)$ is the normal elliptic integral of the first kind. Also,

$$\psi = \arcsin \sqrt{\frac{r_b - r_d}{r_a - r_c}}, \quad (\text{A.2})$$

$$k^2 = \frac{(r_a - r_d)(r_b - r_c)}{(r_a - r_c)(r_b - r_d)}, \quad (\text{A.3})$$

where $r_a = r_{\min}$, r_b , r_c , r_d ($r_a > r_b > r_c > r_d$) are the roots of $R(r) = 0$. For the radial integral of Eq. (11) we have:

$$\begin{aligned}
 L(\lambda, \eta) &\equiv 2 \int_{r_{\min}}^{\infty} \frac{a(2r - a\lambda)}{\Delta \sqrt{R(r)}} dr \\
 &= 2a \sum_{i=1}^2 K_i \int_{r_{\min}}^{\infty} \frac{dr}{(r - r_i) \sqrt{R(r)}} \\
 &= g \sum_{i=1}^2 \Gamma_i [(1 - \beta_i^2) \Pi(\psi, \alpha_i^2, k) + \beta_i^2 F(\psi, k)], \quad (\text{A.4})
 \end{aligned}$$

where $\Pi(\psi, \alpha^2, k)$ is the normal elliptic integral of the third kind and

$$r_i = 1 + (-1)^{i+1} \sqrt{1 - a^2}, \quad (\text{A.5})$$

$$K_i = 1 + (-1)^{i+1} \frac{1 - a \lambda/2}{\sqrt{1 - a^2}}, \quad (\text{A.6})$$

$$\Gamma_i = \frac{K_i}{r_a - r_i}, \quad (\text{A.7})$$

$$\alpha_i^2 = \frac{(r_i - r_b)(r_a - r_d)}{(r_i - r_a)(r_b - r_d)}, \quad (\text{A.8})$$

$$\beta_i^2 = \frac{r_i - r_a}{r_i - r_b}, \quad (\text{A.9})$$

$$g = \frac{4a}{\sqrt{(r_a - r_c)(r_b - r_d)}}. \quad (\text{A.10})$$

These expressions are only valid for $a \neq 1$. For $a = 1$ we have:

$$\begin{aligned} L(\lambda, \eta) &= 2 \int_{r_{\min}}^{\infty} \left[\frac{2 - \lambda}{(r - 1)^2} + \frac{2}{r - 1} \right] \frac{dr}{\sqrt{R(r)}} \\ &= \frac{g}{r_a - 1} \left\{ \beta^2 \left[2 + \frac{\beta^2(2 - \lambda)}{r_a - 1} \right] F(\psi, k) + 2(1 - \beta^2) \left[1 + \frac{\beta^2(2 - \lambda)}{r_a - 1} \right] \Pi(\psi, \alpha^2, k) + \frac{(1 - \beta^2)^2(2 - \lambda)}{r_a - 1} V \right\}, \end{aligned} \quad (\text{A.11})$$

where

$$V = \frac{1}{2(\alpha^2 - 1)(k^2 - \alpha^2)} \left[\alpha^2 E(u) + (k^2 - \alpha^2)u + (2\alpha^2 k^2 + 2\alpha^2 - \alpha^4 - 3k^2) \Pi(\psi, \alpha^2, k) - \frac{\alpha^4 \text{sn } u \text{ cn } u \text{ dn } u}{1 - \alpha^2 \text{sn}^2 u} \right], \quad (\text{A.12})$$

$$u = F(\psi, k), \quad (\text{A.13})$$

$$\alpha^2 = \frac{(1 - r_b)(r_a - r_d)}{(1 - r_a)(r_b - r_d)}, \quad (\text{A.14})$$

$$\beta^2 = \frac{1 - r_a}{1 - r_b}. \quad (\text{A.15})$$

Here $E(u)$ is the complete elliptic integral of the second kind, and sn, cn, dn are the Jacobian elliptic functions.

2. Angular integrals

We begin by defining $u \equiv \cos^2 \theta$, such that

$$\sin \theta d\theta = -\frac{1}{2} \text{sign}(\pi/2 - \theta) \frac{du}{\sqrt{u}}. \quad (\text{A.16})$$

Since all angular integrals considered in this paper are symmetric around $\theta = \pi/2$, we can restrict our interval to $\pi/2 \leq \theta \leq \pi$ and discard the sign of Eq. (A.16) (remember that all integrals are positive definite). However, we need to compensate for the case of a photon that crosses the equator. To this end we define the operator

$$\theta_1 * \theta_2 \equiv \cos \theta_1 \cos \theta_2, \quad (\text{A.17})$$

for any two angles θ_1 and θ_2 . Is clear that $\theta_1 * \theta_2 > 0$ if both angles are at the same hemisphere and negative

otherwise. Therefore, is easy to show that we can write

$$\pm \int_{\theta_1}^{\theta_2} = \int_{\underline{u}}^{\bar{u}} + [1 - \text{sign}(\theta_1 * \theta_2)] \int_0^{\underline{u}}, \quad (\text{A.18})$$

where $\underline{u} = \min(u_1, u_2)$ and $\bar{u} = \max(u_1, u_2)$.

In the trajectories that we consider in this article the photon encounters various turning points defined by: $\Theta(\theta) = 0$. The positive solution to this equation is [see Eq. (6)]:

$$u_m = \frac{1}{2} \left\{ 1 - \frac{\lambda^2 + \eta}{a^2} + \left[\left(1 - \frac{\lambda^2 + \eta}{a^2} \right)^2 + 4 \frac{\eta}{a^2} \right]^{1/2} \right\}, \quad (\text{A.19})$$

where the subscript “m” stands for “min/max”. The corresponding angles are

$$\theta_{\min/\max} = \arccos(\pm \sqrt{u_m}), \quad (\text{A.20})$$

where the plus sign correspond to θ_{\min} and the negative to θ_{\max} .

Now, for a trajectory that encounters m turning points ($m \geq 1$) we have

$$\begin{aligned} \pm \int_{\theta_s}^{\theta_{\min/\max}} & \pm \underbrace{\int_{\theta_{\min/\max}}^{\theta_{\max/\min}} \pm \int_{\theta_{\max/\min}}^{\theta_{\min/\max}} \cdots \pm \int_{\theta_{\max/\min}}^{\theta_o}}_{m-1 \text{ times}} \\ & = \int_{u_s}^{u_m} + [1 - \text{sign}(\theta_s * \theta_{ms})] \int_0^{u_s} \\ & + \int_{u_o}^{u_m} + [1 - \text{sign}(\theta_o * \theta_{mo})] \int_0^{u_o} \\ & + 2(m-1) \int_0^{u_m}, \end{aligned} \quad (\text{A.21})$$

where

$$\theta_{mo} \equiv \arccos[\text{sign}(y_i) \sqrt{u_m}], \quad (\text{A.22})$$

$$\theta_{ms} \equiv \begin{cases} \theta_{mo}, & m \text{ odd}; \\ \pi - \theta_{mo}, & m \text{ even}, \end{cases} \quad (\text{A.23})$$

with y_i as the (possible) position of the image. In deriving Eq. (A.21) we have use the fact that, as discussed in section III, $u_m \geq u_s, u_o$. For $m = 0$ we can write

$$\begin{aligned} \pm \int_{\theta_s}^{\theta_o} & = \int_{\underline{u}}^{\bar{u}} + [1 - \text{sign}(\theta_s * \theta_o)] \int_0^{\underline{u}} \\ & = \int_{\underline{u}}^{u_m} - \int_{\bar{u}}^{u_m} + [1 - \text{sign}(\theta_s * \theta_o)] \int_0^{\underline{u}}, \end{aligned} \quad (\text{A.24})$$

where $\underline{u} = \min(u_s, u_o)$ and $\bar{u} = \max(u_s, u_o)$.

To write the angular integrals of Eq. (10) as elliptic integrals we change variables to u so that, for θ_j and $\theta_{\min/\max}$ in the same hemisphere, we have

$$\begin{aligned} \int_{\theta_j}^{\theta_{\min/\max}} \frac{d\theta}{\pm \sqrt{\Theta(\theta)}} & = \frac{1}{2|a|} \int_{u_j}^{u_m} \frac{du}{\sqrt{u(u_m - u)(u - u_3)}} \\ & = h F(\Psi_j, \kappa), \end{aligned} \quad (\text{A.25})$$

where

$$h = \frac{1}{|a| \sqrt{u_m - u_3}}, \quad (\text{A.26})$$

$$\Psi_j = \arcsin \sqrt{1 - \frac{u_j}{u_m}}, \quad (\text{A.27})$$

$$\kappa^2 = \frac{u_m}{u_m - u_3}, \quad (\text{A.28})$$

$$u_3 = \frac{1}{2} \left\{ 1 - \frac{\lambda^2 + \eta}{a^2} - \left[\left(1 - \frac{\lambda^2 + \eta}{a^2} \right)^2 + 4 \frac{\eta}{a^2} \right]^{1/2} \right\}, \quad (\text{A.29})$$

and $u_m > u_3$ ($u_3 < 0$). On the other hand we have

$$\frac{1}{2|a|} \int_0^{u_j} \frac{du}{\sqrt{u(u_m - u)(u - u_3)}} = h F(\Phi_j, \kappa), \quad (\text{A.30})$$

where

$$\Phi_j = \arcsin \sqrt{\frac{u_j(u_m - u_3)}{u_m(u_j - u_3)}}. \quad (\text{A.31})$$

Using Eqs. (A.21), (A.24), (A.25) and (A.30) we can write the left hand side of Eq. (10) as

$$\begin{aligned} G(\lambda, \eta, \theta_s, m) & \equiv h \{ F(\Psi_s, \kappa) + F(\Psi_o, \kappa) \\ & + [1 - \text{sign}(\theta_s * \theta_{ms})] F(\Phi_s, \kappa) \\ & + [1 - \text{sign}(\theta_o * \theta_{mo})] F(\Phi_o, \kappa) \\ & + 2(m-1) K(\kappa) \}, \end{aligned} \quad (\text{A.32})$$

for $m \geq 1$. Here, $K(\kappa)$ is the complete elliptic integral of the first kind: $K(\kappa) = F(\pi/2, \kappa)$. For $m = 0$ we have

$$\begin{aligned} G(\lambda, \eta, \theta_s, m) & \equiv h \{ F(\underline{\Psi}, \kappa) - F(\bar{\Psi}, \kappa) \\ & + [1 - \text{sign}(\theta_s * \theta_o)] F(\underline{\Phi}, \kappa) \}, \end{aligned} \quad (\text{A.33})$$

where $\underline{\Psi}$ and $\bar{\Psi}$ are given by Eq. (A.27) with the substitutions $u_j \rightarrow \min(u_s, u_o)$ and $u_j \rightarrow \max(u_s, u_o)$ respectively, and $\underline{\Phi}$ is given by Eq. (A.31) with the substitution $u_j \rightarrow \min(u_s, u_o)$.

Now we turn our attention to the angular integrals of Eq. (11). Making the usual change of variable, we get:

$$\begin{aligned} & \int_{\theta_j}^{\theta_{\min/\max}} \frac{d\theta}{\pm \sin^2 \theta \sqrt{\Theta(\theta)}} \\ &= \frac{1}{2|a|} \int_{u_j}^{u_m} \frac{du}{(1-u)\sqrt{u(u_m-u)(u-u_3)}} \\ &= \frac{h}{1-u_m} \Pi(\Psi_j, \gamma^2, \kappa), \end{aligned} \quad (\text{A.34})$$

where

$$\gamma^2 = \frac{u_m}{u_m - 1}. \quad (\text{A.35})$$

The second integral we need is

$$\begin{aligned} & \frac{1}{2|a|} \int_0^{u_j} \frac{du}{(1-u)\sqrt{u(u_m-u)(u-u_3)}} \\ &= \frac{h}{1-u_3} [F(\Phi_j, \kappa) - u_3 \Pi(\Phi_j, \rho^2, \kappa)], \end{aligned} \quad (\text{A.36})$$

where

$$\rho^2 = \frac{u_m(1-u_3)}{u_m - u_3}. \quad (\text{A.37})$$

Using (A.21), (A.24), (A.34) and (A.36) the angular integrals of Eq. (11) become

$$\begin{aligned} J(\lambda, \eta, \theta_s, m) \equiv & \frac{h\lambda}{1-u_m} [\Pi(\Psi_s, \gamma^2, \kappa) + \Pi(\Psi_o, \gamma^2, \kappa)] + \frac{h\lambda}{1-u_3} \{ (1 - \text{sign}(\theta_s * \theta_{ms})) [F(\Phi_s, \kappa) - u_3 \Pi(\Phi_s, \rho^2, \kappa)] \\ & + (1 - \text{sign}(\theta_o * \theta_{mo})) [F(\Phi_o, \kappa) - u_3 \Pi(\Phi_o, \rho^2, \kappa)] + 2(m-1) [K(\kappa) - u_3 \Pi(\rho^2, \kappa)] \}, \end{aligned} \quad (\text{A.38})$$

for $m \geq 1$, and

$$J(\lambda, \eta, \theta_s, m) \equiv \frac{h\lambda}{1-u_m} [\Pi(\underline{\Psi}, \gamma^2, \kappa) - \Pi(\overline{\Psi}, \gamma^2, \kappa)] + \frac{h\lambda}{1-u_3} \{ [1 - \text{sign}(\theta_s * \theta_o)] [F(\underline{\Phi}, \kappa) - u_3 \Pi(\underline{\Phi}, \rho^2, \kappa)] \}, \quad (\text{A.39})$$

for $m = 0$.

For the case of a Schwarzschild black hole ($a = 0$) the angular integrals can be solved in close form since the polynomial in the square root become one of second order:

$$\begin{aligned} & \int_{\theta_j}^{\theta_{\min/\max}} \frac{d\theta}{\pm \sqrt{\Theta(\theta)}} \\ &= \frac{1}{2} \int_{u_j}^{u_m} \frac{du}{\sqrt{\eta u - (\lambda^2 + \eta)u^2}} \\ &= \frac{u_m}{2\sqrt{\eta}} \left[\frac{\pi}{2} + \arcsin \left(1 - 2\frac{u_j}{u_m} \right) \right], \end{aligned} \quad (\text{A.40})$$

where

$$u_m = \frac{\eta}{\lambda^2 + \eta}. \quad (\text{A.41})$$

Similarly,

$$\begin{aligned} & \frac{1}{2} \int_0^{u_j} \frac{du}{\sqrt{\eta u - (\lambda^2 + \eta)u^2}} \\ &= \frac{u_m}{2\sqrt{\eta}} \left[\frac{\pi}{2} - \arcsin \left(1 - 2\frac{u_j}{u_m} \right) \right]. \end{aligned} \quad (\text{A.42})$$

Therefore, using Eqs. (A.21) and (A.24), the right hand

side of Eq. (10) becomes

$$G(\lambda, \eta, \theta_s, m) \equiv \frac{u_m}{2\sqrt{\eta}} \left[2\pi m + \text{sign}(\theta_s * \theta_{ms}) \arcsin \left(1 - 2\frac{u_s}{u_m} \right) + \text{sign}(\theta_o * \theta_{mo}) \arcsin \left(1 - 2\frac{u_o}{u_m} \right) \right], \quad (\text{A.43})$$

for $m \geq 1$, and

$$G(\lambda, \eta, \theta_s, m) \equiv \frac{u_m}{2\sqrt{\eta}} \left\{ \frac{\pi}{2} - \arcsin \left(1 - 2\frac{\bar{u}}{u_m} \right) - \text{sign}(\theta_s * \theta_o) \left[\frac{\pi}{2} - \arcsin \left(1 - 2\frac{u}{u_m} \right) \right] \right\}, \quad (\text{A.44})$$

for $m = 0$.

The angular integrals of Eq. (11) can also be calculated in close form for $a = 0$. For that, is convenient to

introduce a new variable: $w \equiv \sin^2 \theta = 1 - u$. Thus,

$$\begin{aligned} & \int_{\theta_j}^{\theta_{\min/\max}} \frac{d\theta}{\pm \sin^2 \theta \sqrt{\Theta(\theta)}} \\ &= \frac{1}{2} \int_{w_m}^{w_j} \frac{dw}{w \sqrt{-\lambda^2 + (2\lambda^2 + \eta)w - (\lambda^2 + \eta)w^2}} \\ &= \frac{1}{2|\lambda|} \left[\frac{\pi}{2} + \arcsin \left(1 - \frac{2\lambda^2 u_j^2}{\eta(1 - u_j)} \right) \right]. \quad (\text{A.45}) \end{aligned}$$

Similarly, for the $0 \rightarrow u_j$ integration we have

$$\begin{aligned} & \frac{1}{2} \int_{w_j}^1 \frac{dw}{w \sqrt{-\lambda^2 + (2\lambda^2 + \eta)w - (\lambda^2 + \eta)w^2}} \\ &= \frac{1}{2|\lambda|} \left[\frac{\pi}{2} - \arcsin \left(1 - \frac{2\lambda^2 u_j^2}{\eta(1 - u_j)} \right) \right]. \quad (\text{A.46}) \end{aligned}$$

Therefore, the angular integrals of Eq. (11) become

$$J(\lambda, \eta, \theta_s, m) \equiv \frac{\text{sign}(\lambda)}{2} \left[2\pi m + \text{sign}(\theta_s * \theta_{ms}) \arcsin \left(1 - \frac{2\lambda^2 u_s^2}{\eta(1 - u_s)} \right) + \text{sign}(\theta_o * \theta_{mo}) \arcsin \left(1 - \frac{2\lambda^2 u_o^2}{\eta(1 - u_o)} \right) \right], \quad (\text{A.47})$$

for $m \geq 1$, and

$$J(\lambda, \eta, \theta_s, m) \equiv \frac{u_m}{2\sqrt{\eta}} \left\{ \frac{\pi}{2} - \arcsin \left(1 - \frac{2\lambda^2 \bar{u}^2}{\eta(1 - u_o)} \right) - \text{sign}(\theta_s * \theta_o) \left[\frac{\pi}{2} - \arcsin \left(1 - \frac{2\lambda^2 u^2}{\eta(1 - u_o)} \right) \right] \right\}, \quad (\text{A.48})$$

for $m = 0$.

Using the expressions for H , G , L and J given above, the ‘‘lens equations’’ (10) and (11) become:

$$H(\lambda, \eta) - G(\lambda, \eta, \theta_s, m) = 0, \quad (\text{A.49})$$

$$\Delta\phi - L(\lambda, \eta) - J(\lambda, \eta, \theta_s, m) = 0, \quad (\text{A.50})$$

with

$$\Delta\phi = \begin{cases} -\phi_s - 2\pi n & , L + J < 0 \\ 2\pi(n + 1) - \phi_s & , L + J > 0 \end{cases} \quad (\text{A.51})$$

where $n = 0, 1, 2, \dots$ is the number of windings around the z axis, and λ , η and θ_s can be written in terms the observer’s sky coordinates by using Eqs. (21), (22), (23) and (24).

[1] A. Einstein, Science **84**, 506 (1936).

[2] M. Dominik, M. D. Albrow, J.-P. Beaulieu, J. A. R. Cald-

- well, D. L. DePoy, B. S. Gaudi, A. Gould, J. Greenhill, K. Hill, S. Kane, et al., *Planetary and Space Science* **50**, 299 (2002).
- [3] W. Sutherland, *Rev. Mod. Phys.* **71**, 421 (1999).
- [4] K.-H. Chae, A. D. Biggs, R. D. Blandford, I. W. Browne, A. G. de Bruyn, C. D. Fassnacht, P. Helbig, N. J. Jackson, L. J. King, L. V. Koopmans, et al., *Phys. Rev. Lett.* **89**, 151301 (2002).
- [5] R. M. Wald, *General Relativity* (The University of Chicago Press, Chicago, 1984).
- [6] C. W. Misner, K. S. Thorne, and J. A. Wheeler, *Gravitation* (Freeman, New York, 1973).
- [7] H. C. Ohanian, *Am. J. Phys.* **55**, 428 (1987).
- [8] K. S. Virbhadra and G. F. R. Ellis, *Phys. Rev. D* **62**, 084003 (2000).
- [9] V. Bozza, S. Capozziello, G. Iovane, and G. Scarpetta, *Gen. Rel. Grav.* **33**, 1535 (2001).
- [10] V. Bozza, *Phys. Rev. D* **66**, 103001 (2002).
- [11] E. F. Eiroa, G. E. Romero, and D. F. Torres, *Phys. Rev. D* **66**, 024010 (2002).
- [12] M. Sereno, astro-ph/0307243.
- [13] I. Bray, *Phys. Rev. D* **34**, 367 (1986).
- [14] C. T. Cunningham and J. M. Bardeen, *Astrophys. J.* **183**, 237 (1973).
- [15] V. Karas, D. Vokrouhlický, and A. G. Polnarev, *Mon. Not. R. Astron. Soc.* **259**, 569 (1992).
- [16] S. U. Viergutz, *Astron. Astrophys.* **272**, 355 (1993).
- [17] S. U. Viergutz, *Astrophysics and Space Science* **205**, 155 (1993).
- [18] V. Bozza, *Phys. Rev. D* **67**, 103006 (2003).
- [19] B. Carter, *Phys. Rev.* **174**, 1559 (1968).
- [20] P. Schneider, J. Ehlers, and E. E. Falco, *Gravitational Lenses* (Springer Verlag, Berlin, 1992).
- [21] K. P. Rauch and R. D. Blandford, *Astrophys. J.* **421**, 46 (1994).
- [22] D. Richstone, E. A. Ajhar, and R. Bender, *Nature* **395**, A14 (1998).
- [23] P. F. Byrd and M. D. Friedman, *Handbook of Elliptic Integrals for Engineers and Scientists* (Springer Verlag, New York, 1971), 2nd ed.
- [24] Apparently the authors of [8, 9, 10, 11] were not aware of Ref. [7] where, not only the relativistic images for a Schwarzschild black hole were discussed, but analytic approximations for their positions and magnifications were also given.
- [25] Information about MATHEMATICA can be found at www.wolfram.com.
- [26] Note that in Ref. [18] the author use units where $2GM/c^2 = 1$ and, in their notation, $a > 0$ is equivalent to $a < 0$ in our notation.